Available online at www.sciencedirect.com
SCIENCE DIRECT®
Journal of Molecular Catalysis A: Chemical 228 (2005) 97–110
JOURNAL OF MOLECULAR CATALYSIS A: CHEMICAL
www.elsevier.com/locate/molcata

Development and sorption characterization of some model mesoporous and microporous silica adsorbents

J.M. Esparza[a], M.L. Ojeda[a], A. Campero[a], G. Hernández[b], C. Felipe[a], M. Asomoza[a], S. Cordero[a], I. Kornhauser[a], F. Rojas[a,*]

[a] *Departamento de Química, Universidad Autónoma Metropolitana-Iztapalapa, P.O. Box 55-534, México D.F. 09340, Mexico*
[b] *Centro de Física Aplicada y Tecnología Avanzada, Universidad Nacional Autónoma de México, Juriquilla, Querétaro, Mexico*

Available online 10 November 2004

Abstract

Mesoporous and microporous silica substrates, each of these kinds endowed with unique textural characteristics, have been prepared via sol–gel and micelle-templating techniques and characterized through N_2 sorption. Materials consisting of a lattice of cage-like monodisperse cavities interconnected by narrow throats (SBA-16), a set of individual cylindrical pores of about the same size (SBA-15), a network of long sinuous ganglion-like sequences of bulges and throats (mesoporous glass, MG), or microporous arrangements of globular nanoparticles (microporous SiO_2) have been developed. The N_2 sorption isotherms of microporous silica at 76 K correspond to International Union of Pure and Applied Chemistry (IUPAC) type I, while those of mesoporous SBA-16, SBA-15, and MG silica match a type IV with hysteresis loops of types H1 or H2 depending on the regularity and nature of the void elements constituting the substrate. A characteristic common to all kinds of porous SiO_2 solids herein synthesized is the rigidity of the arrangements, since the total pore volumes attain limiting values. Pore-size distributions of mesoporous SiO_2 materials can be calculated by density functional theory (DFT) and sometimes by Barrett–Joyner–Halenda (BJH) methods. The microporous SiO_2 adsorbent depicts a larger amount of big micropores (supermicropores) rather than small micropores (ultramicropores), this being a very useful characteristic for the entrapment and ulterior release of volatile compounds. MG substrates depict a percolation vapor threshold while the SBA-16 material shows a cavitation phenomenon during capillary evaporation. Additional properties of SBA-16, SBA-15, MG silica substrates are studied via primary desorption scanning curves.

Keywords: Microporous SiO_2; SBA-15; SBA-16; Mesoporous glass; Vapor percolation

1. Introduction

A long-standing scientific aim regarding the characterization of porous media is related to the validation of the advancements posed by classical or brand-new theories with respect to the interpretation of capillary phenomena in terms of the pore structure features of model substrates. In recent years, it has been possible to see how very idealized void structures such as systems of independent cylindrical pores or interconnected spherical cavities or even disordered structures gifted with narrow pore-size distributions have come to light. Experimental chemists are now providing a myriad of model systems that are liable to proper interpretation for the part of theoretical researchers.

Among the collection of substances that have been employed to generate model pore systems, silica occupies one of the most prominent of positions. Silica is without a doubt an outstanding material due to its remarkable physicochemical properties [1] that allows it to be used in the form of ultra-low density [2] insulating bricks covering the shell of space shuttles or in more mundane activities such as adsorbents or catalysts. The possibility of achieving a low, regular or an astonishing amount of pores ranging from thousands to trillions of voids per unit mass of SiO_2 in sizes extending from millimeters to Ångstroms [3] makes feasible a wide range of applications by virtue of the variety of surface areas and pore volumes therein developed.

* Corresponding author.
E-mail address: fernando@xanum.uam.mx (F. Rojas).

1381-1169/$ – see front matter © 2004 Elsevier B.V. All rights reserved.
doi:10.1016/j.molcata.2004.09.042

Nomenclature

a	adjacent cylinders center-to-center distance
AB	adsorption boundary curve
A_{BET}	BET surface area
A_t	surface area calculated from a *t*-plot
BdB	Broekhoff–de Boer
d_m	mean pore diameter
$b_{d_{100}}$	wall thickness calculated from d_{100} measurements
BJH	Barrett–Joyner–Halenda pore-size distribution determination method
CPG	controlled pore glass
D	pore diameter
d_{100}	interplanar space of diffraction plane (1 0 0)
DB	desorption boundary curve
DFT	density functional theory
Diol	ethylene glycol
DSBM	Dual Site-Bond Model
E	ethanol
EO	poly(ethylene oxide)
FDU-1	porous material made of large cage-like interconnected cavities
F127	Pluronic triblock co-polymer surfactant
H1–H4	IUPAC's types of sorption hysteresis loops
IUPAC	International Union of Pure and Applied Chemistry
M	methanol
MG	mesoporous glass
P	propanol
PDS	primary desorption scanning curve
PO	poly(propylene oxide)
p/p^0	relative vapor pressure
PSD	pore-size distribution
P104	Pluronic triblock co-polymer surfactant
SBA-15	mesoporous solid made of independent cylindrical pores
SBA-16	cage-like porous solid made of spherical pores interconnected by narrow necks
sm	supermicropores
T	adsorbed layer thickness employed in de Boer's surface area and pore volume determination method
TEOS	tetraethoxysilane
TEM	transmission electron microscope
um	ultramicropores
W	pore width
W_{um}	ultramicropore volume
W_{sm}	supermicropore volume
V^m	volume of micropores
V^p	pore volume
$W_{d_{100}}$	mean pore size calculated from XRD d_{100} measurements
XRD	X-ray diffraction

Greek symbols

α_S	Sing's surface area and pore volume determination method
ε	porosity
σ	standard deviation

A great perspective for SiO_2 materials concerns the induction of porous structures displaying vapor sorption isotherm shapes that can be associated to each of the five types (types I–V) of sorption curves devised by the International Union of Pure and Applied Chemistry (IUPAC) [4]; types I, IV, and V even having the possibility of depicting different hysteresis loop profiles (i.e. H1–H4 shapes) associated to N_2 sorption. Fig. 1 depicts the classification of pore structures [5]. The latter classification is due to the Dual Site-Bond Model (DSBM) of porous media [6], which categorizes void structures in terms of the size distributions of two kinds of void entities sites (cavities, chambers) and bonds (necks, throats) that constitute the void arrangement. The lyophylic or lyophobic nature of the silica surface can nowadays be controlled to different extents by the attachment of suitable functional groups [7,8] in order to create the appropriate surface properties that are required for the generation of substrates that can render the desired type of sorption isotherm. Due to the above reasons, SiO_2 can nowadays be prepared in the form of microporous, mesoporous, or macroporous speci-

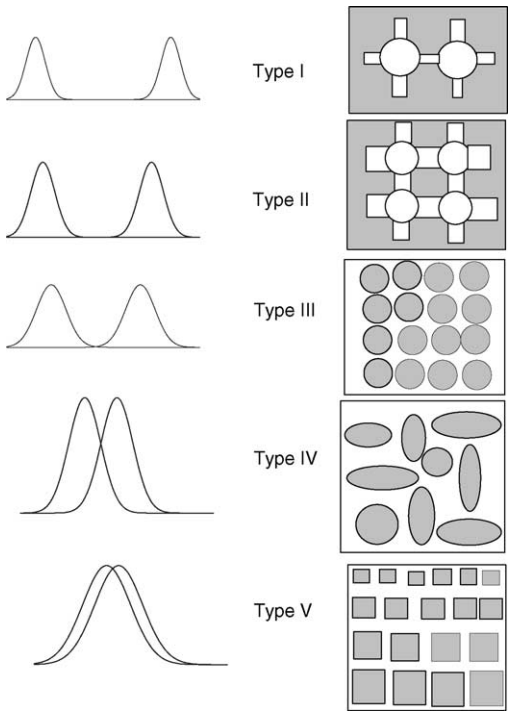

Fig. 1. Classification of porous structures according to the Dual Site-Bond Model. Blank areas correspond to the pores while gray areas correspond to the solid phase.

mens with clean or functionalized surfaces. The pore shape of SiO_2 substrates can be induced via the revolutionary micelle-templating technique [9,10] to eventually obtaining cylindrical, spherical, or slit-like voids regularly arranged throughout a mesoporous and sometimes a microporous solid matrix. In this way, it has been possible to create substrates made of parallel non-intersecting cylindrical mesopores [11–15] (SBA-15) or cage-like structures (SBA-16, FDU-1) [16–19] composed of interconnected spherical cavities. Everyday new developments are continuously increasing the variety of well-defined porous systems.

The idea of this work is to describe the principal pore structure characteristics of some model and typical void structures that are currently employed for the study of diverse phenomena related to surface science and capillary phenomena. First, a brief description of the main structural aspects of SBA-16, SBA-15, MG, and microporous SiO_2 materials synthesized by the sol–gel and micelle-templating methods will be supplied. Afterward, the specific methods of preparation that were employed for the production of these substrates will be succinctly mentioned. Finally, the sorption properties and the exposition of some usual and unusual mechanistic aspects relative to the sorption phenomena developed in these model systems will be undertaken.

1.1. Description of the geneses and porous structures of some model and typical silica substrates

1.1.1. SBA-16 cage-like porous material

This silica material has outstanding properties as it consists of a regular arrangement of interconnected spherical cavities of about the same sizes. This substrate is prepared through the micelle-templating technique [9,10] by seeding spherical surfactant aggregates during the synthesis of a SiO_2 sol performed by the hydrolysis of tetraethoxysilane (TEOS). The micelles are later entangled within the ensuing gel environment and can leave holes inside the amorphous silica phase after being eliminated by a subsequent thermal treatment. Large pore cage-type mesoporous silica, designated as SBA-16 [16–18] or FDU-1 [19], can be synthesized in acidic media with poly(ethylene oxide)–poly(propylene oxide)–poly(ethylene oxide) triblock co-polymers ($EO_nPO_mEO_n$ for brevity) and TEOS as the silica source. Typical cage-like substrates consist of spherical cavities of 6–10 nm in diameter arranged in the form of a body-centered cubic array (i.e. with *Im*3*m* symmetry), and connected through mesoporous openings of 2.0–2.5 nm which lie along the crystallographic (1 1 1) plane. Due to the symmetry of the arrangement, each spherical cavity is surrounded by eight neighboring void entities; pairs of nearest neighbor cavities are linked through narrow necks alongside the (1 1 1) direction [16].

The advantage on counting with a SBA-16 material is due to the fact of achieving a real type I porous structure [5] in which big pore entities are delimited by very narrow necks (see Fig. 1). The sorption properties of this kind of porous structures have been predicted a good deal [20,21] thanks to the above structural fact and also because of the spherical shape of the pore cavities.

1.1.2. SBA-15 cylindrical pore material

One of the most striking materials that have made possible the materialization of perhaps the most famous of classical porous structures is indeed the SBA-15 substrate. This material is formed by arrays of individual independent cylindrical pores of diameters between 4 and 8 nm [11,12]. The cylinders are arranged as sets of six collateral elements in hexagonal (honeycomb) packing. The great regularity of pore sizes and the independent nature of these voids have brought to reality two great achievements: (i) the coincidence into one single curve of the pore-size distribution (PSD) results calculated from both the ascending boundary (AB) and descending boundary (DB) curves delimiting the hysteresis loop of the corresponding sorption isotherm, (ii) the realization that the above matching is highly due to the inclusion of the adsorption potential in the methods employed to perform this calculation. This potential arises from the pore walls toward the adsorbed molecules and its inclusion guarantees the calculation of realistic values of the PSD in these cylindrical pore systems. Additionally, it has been realized that the classical Barrett–Joyner–Halenda (BJH) method underestimates the PSD of mesoporous materials having pores smaller than 10 nm by 1 nm or sometimes even more nanometers. Further advantages of characterizing SBA-15 substrates by sorption methods include the calculation of the pore wall thickness and the possibility of making evident some subtle properties of the cylindrical voids such as the sinuosity of the tubes making the arrangement by means of the analysis of sorption scanning curves.

1.1.3. Mesoporous silica glass

Cross and Haynes [22] have optically observed the phase separation that occurs when borosilicate glasses are exposed to high temperatures. Between 500 and 750 °C, a borax-rich phase separates from a silica-rich one; acid or basic leaching can then remove the borax phase. The final product consists of a labyrinthic network of interconnected pore entities distributed inside a solid silica matrix that resembles to a certain extent the ganglion channel system of living beings. The morphology of porous glass can be seen by electron microscopy[1] as an interconnected 3-D network of bulges and throats. Porous Vycor glass corresponds to the so-called controlled pore glass (CPG) family [23], which involves substrates endowed with pores of about uniform (i.e. controlled) sizes, especially when these voids are not too small. The main cause of phase separation in borosilicate glasses is the spontaneous process of fluid–fluid spinoidal decomposition that occurs at elevated temperatures and that leaves two individual interconnected silica and borax phases in coexistence [24,25].

[1] A nice electron micrograph of the structure of porous glass can be seen at the site http://www.cpg-biotech.com/cpgp/.

It is also pertinent to say that due to the way by which solid phase separation occurs, the silica-rich phase remaining after acid etching is delimited by a surface of approximately constant mean curvature. Another important feature of controlled porous glasses prepared from borosilicate compounds is the considerable rigidity of the arrangement; consequently, the ensuing vitreous substrate usually displays a fixed pore volume. Furthermore, the porous glass network is eminently a mesoporous structure (usually involving void widths extending from 4 to 20 nm) with almost no incidence of either micropores or macropores.

A great theoretical development related to the genesis and visualization of the morphology of porous glass is due to Gelb and Gubbins [26,27]. These authors have simulated the phase separation occurring in porous glasses through molecular dynamics; initially, molecules of two types A and B are randomly seeded to start creating a precursor glass substrate. Interaction potentials between molecule pairs are established in terms of van der Waals forces; an unbalance between A–A and B–B interactions with respect to weaker A–B interactions represents the driving force for phase separation. The final phase configuration is similar to that arising from borosilicate glasses. Afterward, one of the clusters formed by the same type of molecules (i.e. A–A–A··· or B–B–B···) is taken away from the particle conglomerate to finally obtaining an interconnected porous glass structure.

The sol–gel method [28] constitutes nowadays an alternative route to synthesize porous silica glasses without involving the deployment of excessively high temperatures; additionally, this experimental technique allows controlling to a certain extent the sizes of the solid particles constituting the silica xerogel, which after calcination leads to the final porous glass material.

1.1.4. Microporous SiO_2 material

Both sol–gel [29] and micelle-templating [30] techniques can produce microporous SiO_2. The genesis of such material starts with the creation of solvated SiO_4 tetrahedral species, which then polymerize to form a gel [2]. The final result after the drying and calcination of the precursor SiO_2 gel is a vitreous silica skeleton in which a network of pores of various sizes and shapes is intertwined. During the gelation process, SiO_4 tetrahedrons aggregate in the form of a silica network to make primary particles of 3–10 nm diameters. Eventually, these particles cluster in a fractal packing on length scales ranging from 6 to 100 nm. Because of its large surface area (this pore structure parameter that can sometimes attain values larger than 960 $m^2\,g^{-1}$), significant pore volume ($\sim$1 $cm^3\,g^{-1}$), high thermal stability, and rigid structure, microporous SiO_2 is a suitable adsorbent for both small and bulky molecules [31]. An additional valued characteristic of SiO_2 microporous adsorbents is the possibility of introducing metal species (e.g. Ag, Pt, etc.) into the structure during the sol–gel synthesis to render highly dispersed catalytic materials. Two micropore kinds are usually incumbent in SiO_2 substrates: the ultramicropores (i.e. a pore width of less than 0.7 nm) and the supermicropores (a pore width between 0.7 and 2 nm). These latter voids are believed to be rigid interparticle pores caused by primary corpuscle agglomeration [32] and which appear after the drying process of the silica gel microstructure [33].

Microporous silica materials have been prepared in the form of microporous spheres [34], by incorporating porogenic agents within the SiO_2 structure either by co-hydrolysis of two alkoxide compounds, as for instance 3-aminopropyltriethoxysilane and TEOS, or by the incorporation of an organic compound (glycerol) in the gel structure. A microporous silica structure results after calcination of the porogenic organic compounds. A computer visualization of the structure of microporous SiO_2 has been performed already [2].

2. Experimental

2.1. Materials

- TEOS (Aldrich, 98%) was employed in all SiO_2 syntheses.
- Ethanol analytical grade (Aldrich, 99.8 wt.%) was used in all SiO_2 syntheses. Methanol and propanol of similar analytical purity as ethanol were utilized for the preparation of microporous SiO_2.
- Pluronic P104 $(EO)_{27}(PO)_{61}(EO)_{27}$ and Pluronic F127 $(EO)_{106}(PO)_{70}(EO)_{106}$ triblock co-polymers obtained from BASF were used for the synthesis of SBA-15 and SBA-16 materials.
- HCl (Monterrey, 38%) was required for the syntheses of SBA-16 and SBA-15.
- $Fe(NO_3)_3{\cdot}9H_2O$ (Aldrich, 99.99%), $CuCl_2{\cdot}2H_2O$ (Aldrich, 99.99%), and ethylene glycol were reactants employed in the synthesis of CPG substrates.
- Ultra-high purity N_2 and He gases (99.99%; Praxair) were selected to perform the sorption experiments on all silica materials.
- A natural non-porous α-quartz solid was required as a reference substrate for the estimation of the micropore volumes of microporous silica samples.

All chemicals were used as supplied without further purification.

2.2. Preparation and characterization of assorted silica substrates

2.2.1. Cage-like SBA-16 silica

An amount of 1.6 g (1.26×10^{-4} mol) of Pluronic F127 was mixed with 2.6 cm^3 of HCl 0.037 M at room conditions; afterward, 12.2 cm^3 (0.2096 mol) of ethanol was incorporated to the latter system. The mixture was kept under stirring to attain a homogeneous solution and then 3.6 cm^3 of TEOS was added dropwise; the stirring rate was maintained for further 5 h. The theoretical molar composition of the ensuing sol was

as follows: 1TEOS:9H_2O:0.006HCl:13.1EtOH:0.0079F127. Finally, the above sol was allowed to gelify at room conditions during a period of about 2 weeks. A transparent, monolithic and rigid specimen was finally obtained; the monolith was cut into several pieces, which were washed with distilled water and treated at 500 °C during 6 h (a heating ramp of 1° min^{-1} was chosen).

N_2 sorption isotherms at 76 K were measured via a Quantachrome Autosorb-1 instrument. The sample was outgassed overnight at 473 K. Adsorption and desorption boundary curves as well as primary descending scanning curves measured at different points of reversal were determined to characterize the SBA-16 material.

TEM images of the SBA-16 material were taken by means of a JEM-2010F FASTEM instrument.

2.2.2. SBA-15 cylindrical pore substrate

The SBA-15 silica material was synthesized as follows. 1.5 g of Pluronic P104 block co-polymer was dissolved in 48 cm^3 of an aqueous HCl 2 M solution. The temperature of the solution was then raised to 323 K and 3.7 cm^3 of TEOS was added drop-by-drop to the above mixture while the system was being subjected to a vigorous stirring for 5 min. The stirring rate was then lowered down and kept under this condition for further 24 h. Subsequently, the reaction beaker holding the reacting mixture was placed inside a sand-containing heating mantle and heated up to 80 °C during approximately 48 h. The ensuing white precipitate was separated from the liquid phase by filtering and washed abundantly with deionised water. Afterwards, more residual surfactant was removed from the as-synthesized solid product by slurring this specimen in 40 cm^3 of a 50 vol.% ethanol/H_2O solution for 2 h, after which time it was once more filtered and washed with distilled water and later dried at 373 K to be finally calcined in air for 6 h at 823 K (heating rate 1° min^{-1}). The nominal molar composition of the synthesized gel was 1TEOS:158H_2O:6HCl:0.016Pl04.

The SBA-15 material was characterized by transmission electron microscopy (TEM) employing a Leo EM-910 instrument operated at 120 kV.

A N_2 sorption isotherm at 76 K was measured by means of a Quantachrome Autosorb-1 automatic volumetric instrument. The sample was degassed at 250 °C for 8 h previously to the adsorption run.

2.2.3. Mesoporous silica glass

The synthesis of MG substrates was performed in a glass round-bottom flask kept at room temperature (298 K) by dissolving 37.9 cm^3 of TEOS in 59 cm^3 of ethanol under gentle magnetic bar stirring. Afterward, the amount of water necessary to carry out the hydrolysis reaction (12 cm^3) was added together with some drops of HF and HCl acids; the stirring was continued for further 30 min. Subsequently, the resulting sol was poured into a glass cylinder where gelation eventually occurred. One of the silica monoliths (hereafter labeled as SiO_2–diol) was prepared under the presence of a diolic agent by using the same amounts of the above reactants but this time including 14 cm^3 extra of ethylene glycol which were added to the TEOS–ethanol solution prior to its mixing with water. All gels were dried in an oven at 383 K for 48 h. The final xerogels were obtained in the form of soft, gelatinous but consolidated (i.e. no fractures were observed) cylindrical masses that could be easily removed from the glass cylinders. These xerogels were calcined at 773 K during 10 h to finally obtain a series of mesoporous silica rigid cylindrical monoliths.

Fe and Cu-doped silica monoliths were synthesized in the same way as the pure silica specimens. In the case of SiO_2–Fe monoliths, the iron source was 1.3 g of $Fe(NO_3)_3{\cdot}9H_2O$, a mass that was introduced together with the water employed for the reaction. For the SiO_2–Cu materials, the copper source was 0.56 g of $CuCl_2{\cdot}2H_2O$. The drying and calcination procedures of Fe and Cu-doped SiO_2 monoliths were the same as those employed for the pure silica substrata.

An automatic Quantachrome Autosorb-1 sorption apparatus was used to obtain the isotherms of the SiO_2–Cu, SiO_2–Fe, and SiO_2–diol glasses. Samples were outgassed at 573 K for 10 h and stored under helium previously to the adsorption run.

2.2.4. Microporous SiO_2

Microporous silica monoliths were synthesized as follows. TEOS was first dissolved in the selected alcohol (methanol (M), ethanol (E), or propanol (P)) and then mixed with deionized water according to the ratio 1TEOS:4alcohol:2.5H_2O. Each reactant mixture was prepared inside a glass column that was maintained at 303 K for several days, during which the sol–gel hydrolysis–condensation reactions took place. The resulting sols were kept in the original glass columns so that gelation occurred eventually (i.e. a period of 3–4 months was usually required). The ensuing gel was then dried in situ at 373 K for 48 h so that cylindrical monoliths of microporous silica were finally attained. The specimens that were prepared, namely SiO_2–M (methanol being used as the TEOS solvent), SiO_2–E (TEOS dissolved in ethanol), and SiO_2–P (propanol being the TEOS solvent), displayed a significant surface area to pore volume quotient, a characteristic that facilitates the occurrence with great effectiveness of important physical and chemical processes. As will eventually be evident, the microporous SiO_2 materials synthesized here are suitable for high temperature industrial applications and transport of volatile compounds captured inside their pores for posterior release.

N_2 sorption isotherms were measured on microporous solids at 76 K (i.e. the boiling point of liquid nitrogen at 2200 m of Mexico City) in an automatic volumetric adsorption system (Micromeritics ASAP 2000). Nitrogen adsorption isotherms were determined in the interval of relative pressures, p/p^0, extending from 10^{-3} to 0.995. The saturation pressure, p^0, was continuously registered in the course of the adsorption–desorption measurements. Powder particle sizes corresponding to 60–80 mesh were sampled from all

specimens under analysis. Prior to the sorption experiments, solids were outgassed at 623 K for 20 h at a pressure of about 10^{-6} mbar.

3. Results and discussion

3.1. SBA-16 substrate

This substrate means a really good opportunity to test several predictions that have been made with respect to type I porous structures. This kind of solids possesses very small throats linked to large cavities; therefore, during the development of the AB curve, necks fill with condensate well in advance of sites. In turn, these latter voids fill sequentially from smaller to larger sizes. A proper analysis of the AB curve (i.e. if assuming spherical menisci and if taking into account the adsorption potential) should lead to convincing values of the site size distribution. Since the SBA-16 material is made from a well-known surfactant (F127) which forms monodisperse spherical micelles with hard-core dimensions of about 9 nm (this quantity corresponds to the size of the $(PO)_{70}$ hydrophobic micelle core) [35], a magnitude of this sort would be expected for the mean value of the PSD inferred from adsorption data. The spherical shape of the chambers would also allow the calculation of the number of sites of the SBA-16 adsorbent considering that the volume of bonds is almost negligible. Interesting too would be to know if the Kiselev equation [36] can render appropriate values of the mesopore surface area. In the next paragraphs, an attempt to clarify all the above premises will be undertaken.

Let us start providing the values of some main pore structure parameters of the SBA-16 cage-like solid. These quantities were derived from the analysis of the N_2 isotherm (Fig. 2) and are given in Table 1. Several points deserve attention:

- The N_2 hysteresis loop is a wide cycle depicting a plateau; the isotherm shape is proper of a type I porous structure [5] while the hysteresis cycle corresponds to a type H2 [4]. This hysteresis shape involves a vapor percolation threshold of the DB curve occurring at a p/p^0 value around 0.42 thus meaning that a cavitation phenomenon is taking place [37,38]. This latter phenomenon consists in the nucleation of bubbles within the liquid-like condensed phase thus allowing an abrupt release of most of the totality of this latter phase toward the bulk vapor surrounding the sample.
- The pore size distribution was obtained from the adsorption branch of the N_2 isotherm by means of a BJH treatment [39] that employs a Broekhoff–de Boer (BdB) corrected Kelvin equation [40] to render the curve shown in Fig. 3. The mean cavity size happens to be 8.9 nm, a value very close to the expected 9 nm hard-core size of the F127 micelle. The bond size distribution is not possible to be evaluated from desorption data due to the cavitation phenomenon. Note also that the PSD has a certain standard deviation (0.71 nm), this fact then causing the sloping shape of the AB curve. The mean cavity size can also be calculated from the XRD pattern knowing that the main (1 1 1) signal appears at 0.99° (see Fig. 4) and supposing that the cavities are connected to each other by narrow volumeless windows. In this way the XRD calculation renders a value of 8.9 nm a magnitude very close to the sorption and hard core micelle values.

Table 1
Pore structure parameters of SBA-16 silica determined from N_2 sorption and XRD

BET area ($m^2\ g^{-1}$)	256
Mesopore area ($m^2\ g^{-1}$)	177
Micropore area ($m^2\ g^{-1}$)	79
Kiselev mesopore area ($m^2\ g^{-1}$)	169
Total pore volume ($mm^3\ g^{-1}$)	293
Mesopore volume ($mm^3\ g^{-1}$)	259
Micropore volume ($mm^3\ g^{-1}$)	34
BdB–BJH mean pore size $\pm 1\sigma$ (nm)	8.9 ± 0.71
XRD mean pore width (nm)	8.9
Spherical cavity number (g^{-1})	1.77×10^{20}

σ: Standard deviation.

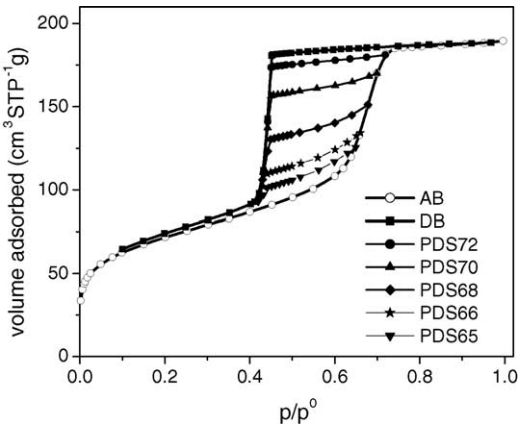

Fig. 2. N_2 sorption isotherm at 76 K on sample SBA-16. Boundary (AB, DB) and primary desorption scanning (PDS) curves are plotted. The numeric labels of the PDS curves correspond to $100p/p^{0*}$, where p/p^{0*} represents the vapour pressure at the point of reversal of the PDS path.

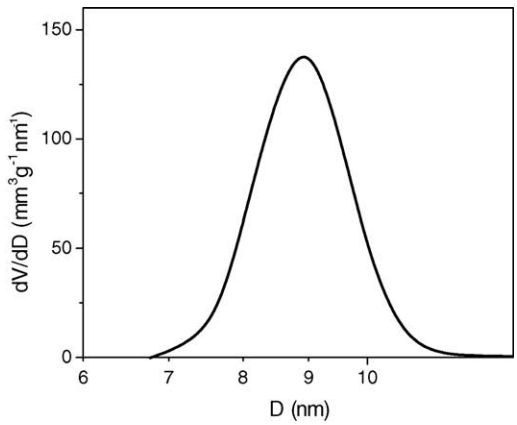

Fig. 3. Site-size distribution of simple SBA-16 determined from N_2 adsorption.

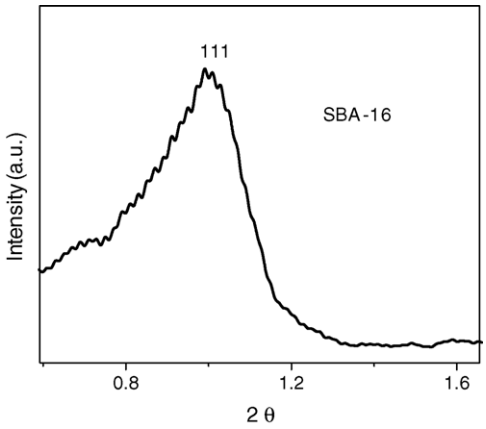

Fig. 4. XRD diffraction pattern of sample SBA-16.

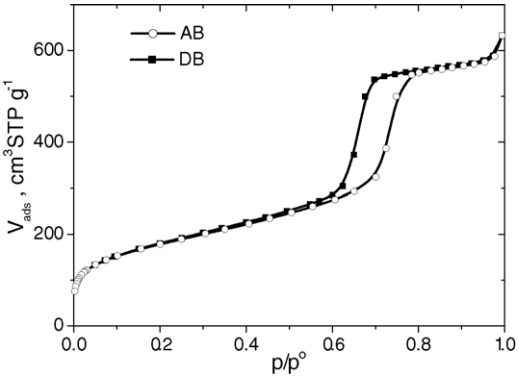

Fig. 6. N_2 sorption at 76 K on SBA-15 (first lot) substrate.

- The structure can be regarded as a type I in the Mayagoitia's classification [5], this assertion is supported by the appearances of the boundary ascending and descending curves as well as by the aspect of primary desorption scanning curves (PDS). The filling of the cage-like structure of the SBA-16 material starts with the development of an adsorbed layer on the walls of all pore entities; at certain stage during the development of the isotherm the necks become filled of condensate due to their small sizes; at higher vapor pressures the cavities start to be occupied by condensate according to their sizes. Desorption along the descending boundary curve first occurs gently from the saturation point downward to some critical point at which cavitation takes place abruptly and most of the liquid is removed from the pores. The nucleation of bubbles would take place at points located on the wall delimiting the pore cavities rather than in the core of the condensed phase [41].
- The *t*-method [42] indicates that the SBA-16 sample includes a certain amount of micropores (34 mm^3). These micropores can be due to the occlusion of individual or small clusters of surfactant molecules within the mass of the SiO_2 substrate; these occluded molecules can be located around the zone at which two spherical cavities communicate with each other and can even be the cause of some tunneling between contiguous cavities [43]. The low-pressure hysteresis region depicted by the N_2 isotherm from $p/p^0 = 0.4$ downwards may also be an indication of the existence of these micropores [4]. Another important fact about the *t*-plot is that the area due to mesopores amounts to 177 $m^2\ g^{-1}$ and that capillary condensation starts occurring at $p/p^0 = 0.55$ approximately (at which point the *t*-curve starts showing a noticeable upward deviation).
- The Kiselev equation [36] has been used in the form given by Broekhoff and de Boer [44] to calculate the area due to mesopores. This area calculation renders a value of 169 $m^2\ g^{-1}$ that is close to that provided by the *t*-plot (176 $m^2\ g^{-1}$). The quantity of condensed phase that is involved in this method is negligible up to $p/p^0 = 0.55$, therefore the Kiselev area method is taking into account only the cavities that are filling from this relative pressure onwards.

TEM photographs (Fig. 5) show some interesting aspects about the spherical cavities that form this regular porous arrangement as well as some of the crystal planes related to the body-centered cubic configuration of the SBA-16 sample.

3.2. SBA-15 substrate

The sorption isotherm (Fig. 6) of the SBA-15 solid indicates a type IV isotherm and a type H1 hysteresis loop for

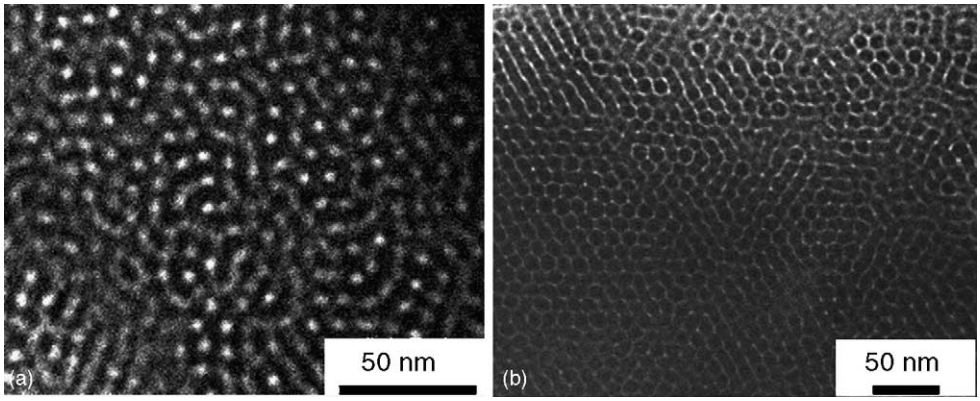

Fig. 5. TEM micrographs of sample SBA-16. (a) Regular distribution of pore cavities, (b) arrangement of neighboring cavities.

Table 2
Pore structure parameters of sample SBA-15 determined from N_2 sorption and XRD

BET area ($m^2\ g^{-1}$)	645
Mesopore *t*-area ($m^2\ g^{-1}$)	491
DFT-DB mesopore area ($m^2\ g^{-1}$)	477
Micropore area ($m^2\ g^{-1}$)	154
Total pore volume ($mm^3\ g^{-1}$)	890
Mesopore volume ($mm^3\ g^{-1}$)	828
Micropore volume ($mm^3\ g^{-1}$)	62
DFT-AB mean pore size $\pm 1\sigma$ (nm)	7.59 ± 0.71
DFT-DB mean pore size $\pm 1\sigma$ (nm)	7.90 ± 0.5
XRD mean pore size, $W_{d_{100}}$ (nm)	8.08
Interplanar space, d_{100} (nm)	10.11
Adjacent cylinders center-to-center distance, *a* (nm)	8.12
Wall thickness, $b_{d_{100}}$ (nm)	2.03

this sample. These two profiles together with the values of the structural parameters of this material that are listed in Table 2 and the series of TEM photographs shown in Fig. 7a–c indicate that this solid is preponderantly a co-acervate of cylindrical mesopores of fairly uniform diameters. The BET surface area is 645 $m^2\ g^{-1}$ of which 491 $m^2\ g^{-1}$ is due to mesopores; this latter quantity as well as the micropore volume (62 $mm^3\ g^{-1}$) was obtained from the corresponding *t*-plot [42]. Therefore, besides of cylindrical capillaries occupying a volume of 828 $mm^3\ g^{-1}$ there exist a certain amount of intrawall micropore channels [43] within a total pore volume of 890 $mm^3\ g^{-1}$. Finally, it will be pertinent to mention that the density functional theory (DFT)-DB mesopore area of the SBA-15 sample renders 477 $m^2\ g^{-1}$ and that the onset of capillary condensation in SBA-15 is located at about $p/p^0 = 0.65$ according to the *t*-plot.

Cylindrical pore diameters with means of 7.59 and 7.90 nm were obtained by applying the DFT treatment [45,46] to the AB and DB isotherm curves, respectively (see Fig. 8). The XRD pattern (Fig. 9) depicts a distinctive diffraction band corresponding to the (1 0 0) plane while less intense signals can be attributed to (1 1 0) and (2 0 0) planes. A mean pore diameter of 8.08 nm was calculated by means of the Kruk–Jaroniec procedure [47] and an average wall thickness

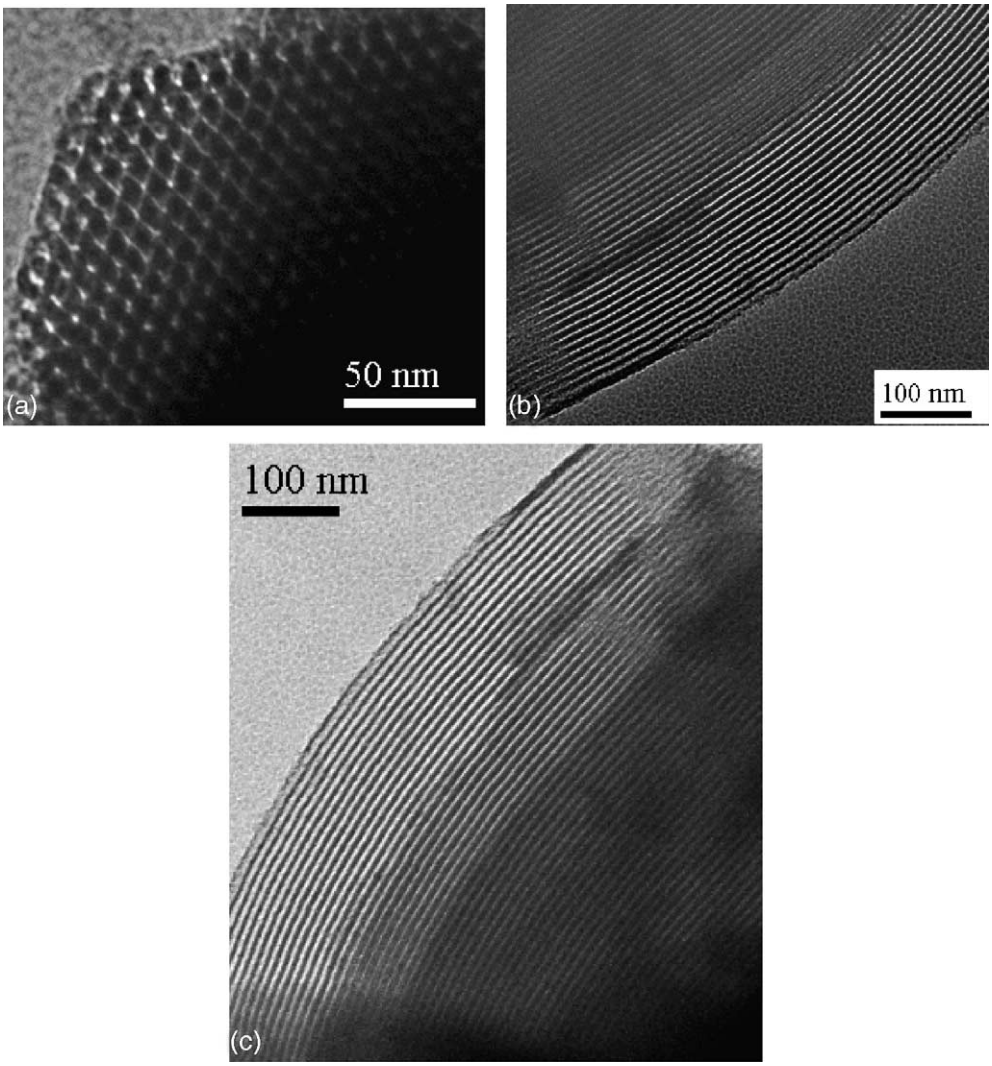

Fig. 7. TEM photographs of sample SBA-15. Pore mouths (top, LHS), pore walls (top, RHS), and curved pore walls (bottom) of cylindrical pores.

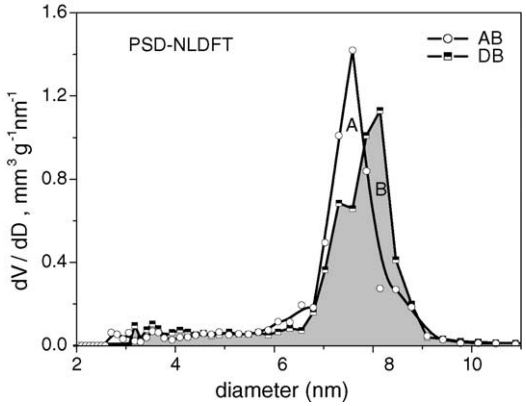

Fig. 8. Pore-size distributions measured from N_2 sorption on simple SBA-15. AB: adsortion boundary curve, DB: desorption boundary curve.

of 2.03 nm has been obtained from the XRD pattern, thus a very good agreement has been found with the DFT-DB result.

The fit between AB- and DB-DFT PSD curves is fine but not perfect. The reason for this may be due to some sinuosity of the cylindrical pores of the SBA-15 material. When having a close look of the pore walls (see Fig. 7), it is evident that the capillaries are not perfect, straight cylinders but some wall deformation and bending in the form of U-turns exist in this material. This sinuosity causes the existence of bulges and throats (see Fig. 10) and as explained by Everett [48] the filling of a bulge in a tubular system can be caused by the formation of liquid–gas menisci at the necks surrounding such cavity. Once these menisci are formed then can advance straightforwardly into the bulges replenishing them with condensate. This phenomenon is called *advanced adsorption* [49] and causes that, during the development of the AB curve, tubular pores can fill at relative pressures smaller than those required for condensation to occur in individual bulges. The advanced filling of bulges along the AB isotherm and the delayed emptying of these same cavities down the DB curve (by reason of the pore blocking created by the delimiting throats of the cavity) causes that the area marked as A in Fig. 8 is about the same as the area marked as B in the same figure. Consequently, advanced adsorption is a possible explanation of why the PSD curve calculated from the AB curve is somewhat shifted toward smaller pore diameters than the PSD outcome proceeding from the BD isotherm.

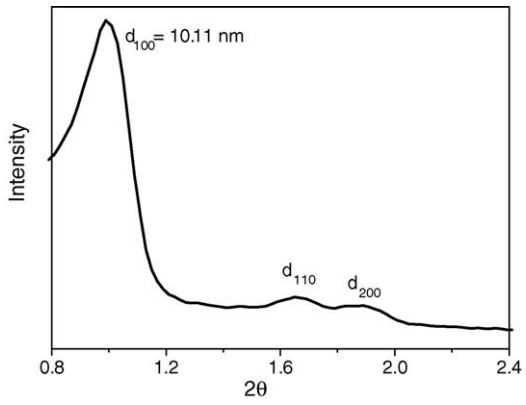

Fig. 9. XRD spectrum of simple SBA-15 showing distinctive bands.

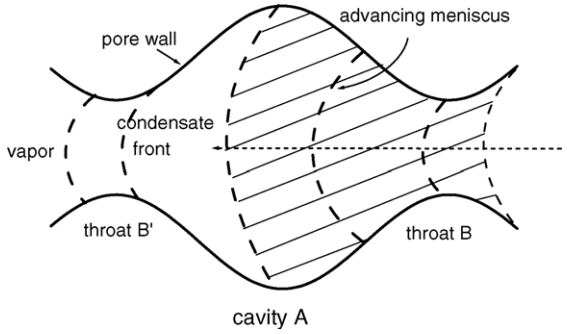

Fig. 10. Schematic representation of a sequence of bulges (cavity A) and necks (throats B–B′) inside a tubular pore. Condensation of vapor at throat B produces the advancement of a hemispherical liquid–vapor meniscus into cavity A and then into throat B′.

A second lot of sample SBA-15 was employed to determine a set of PDS curves (Fig. 11). The appearance of these scanning isotherms underlines the fact that this porous system is an assortment of independent cylindrical pores: each of these paths approaches straightforwardly the DB isotherm, since there are no pore network interconnection effects in this sample. Contrastingly, as we will see later for the case of mesoporous glasses, a PDS curve associated to these substrates approaches the BD curve in a much more steadily and asymptotic way.

3.3. Mesoporous silica glasses

As mentioned before mesoporous silica glasses have been traditionally acknowledged as consisting of an interconnected void network that display cavities (i.e. chambers, sites, antræ) linked to each other through narrower throats (necks, bonds, capillaries) thus conforming a non-independent pore arrangement. The sorption isotherms of porous glasses match

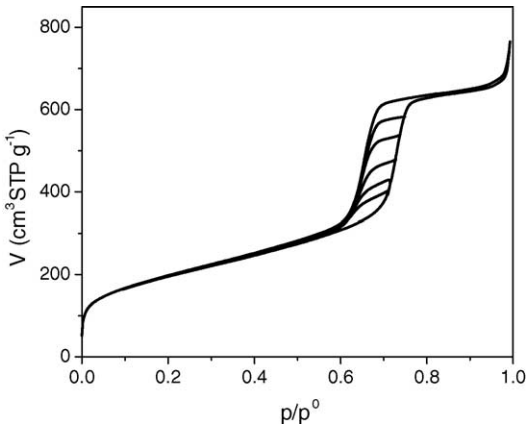

Fig. 11. N_2 sorption isotherm on sample SBA-15 (second lot). Boundary and primary descending scanning curves are shown.

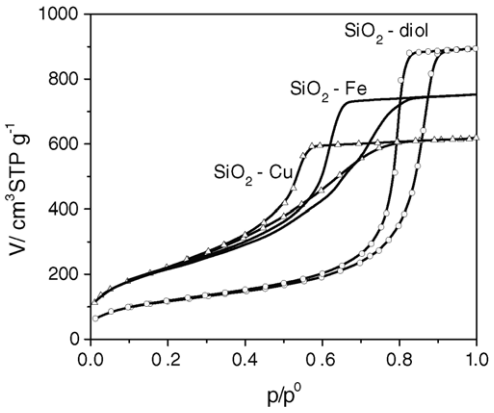

Fig. 12. N_2 sorption isotherms at 76 K on mesoporous glasses.

IUPAC types H1 or H2 hysteresis loops [4]. Depending on the relative sizes of sites and bonds, it can happen that the outcome of the AB isotherm could be controlled by condensation in either sites or bonds, while condensate evaporation from bonds would be in control of most of the volume desorbed along the DB path.

N_2 sorption isotherms at 76 K determined on samples SiO_2–Cu, SiO_2–Fe, and SiO_2–diol are shown in Fig. 12; the resultant surface areas and pore volumes are listed in Table 3. All these isotherms correspond to a type IV in the IUPAC classification. One of the first things to note is that the surface areas and porosities of the various porous glasses prepared by the sol–gel procedure are significantly large. The three isotherms depict a saturation plateau thus providing confident values of the total pore volumes. Another important observation to note is the absence of micropores in all samples, a characteristic that is evidenced by the negligible *y*-axis intercept depicted by either *t*- or α_S-plots.

N_2 hysteresis loops of SiO_2–Cu and SiO_2–Fe glass substrates match type H2 cycles although the DB curves of these isotherms are sloping rather than steep thus reflecting that, although bonds sizes are still somewhat smaller than sites, this size difference is not as pronounced as in type I porous solids; therefore, a type II or more likely a type IV or V labeling would be more appropriate for these silica glasses. As a consequence of this hysteresis shape, vapor percolation (instead of cavitation) should be taking place during desorption. The AB isotherm is even more sloping than the DB curve and this indicates that the pore cavities of SiO_2–Cu and SiO_2–Fe are filling gradually with condensate according to their pore sizes unless for the occurrence of some advanced adsorption. Another induction about the sloping character of the AB curves of the latter MG samples is that their resultant PSD's should be rather wide.

On the other hand, the hysteresis loop of the SiO_2–diol substrate is of type H1, a characteristic that is typical of CPG and arrangements of monodisperse solid globules, thus meaning that the sizes of neighboring sites and bonds are not now too different; here it would be expected a larger incidence of advanced adsorption if compared to the SiO_2–Cu glass. According to the structural characteristics found for this SiO_2–diol sample (Table 3), the sizes of the precursory colloidal particles that lead to the formation of this porous solid should be larger (while their standard deviations should be relatively small) if compared with the situation occurring in SiO_2–Fe and SiO_2–Cu samples (smaller particles, wider standard deviations). Definitely, the presence of Fe^{3+} or Cu^{2+} ions produces smaller primary colloidal particles than when absent as in the case of the SiO_2–diol sample.

N_2 primary desorption scanning curves are shown in Fig. 13a–c. The appearances of these curves point out to the fact that vapor percolation takes place more gradually along these scanning curves than along the DB curve. This behavior is a manifestation of the fact that a primary desorption path starts at a certain point of reversal at which not all the pores are filled with condensate (this contrasts with the situation of the DB curve that initiates when all pores are already full of condensate). Due to this circumstance, the pore entities that are full of condensate at the onset of a primary desorption process can be emptied of it through shorter and more accessible vapor-filled trajectories [50]. This assertion will be further discussed in the next paragraph.

A PSD analysis of the SiO_2–Cu sample through the NLDFT treatment (by simplifying the tortuous structure of porous glass in terms of cylindrical voids) sheds light about several interesting characteristics. First, the DB curve renders a sharper PSD than the AB path (Fig. 14a), then reflecting the existence of vapor percolation at some narrow p/p^0 region during the development of the DB isotherm. The pore sizes measured from the AB curve are located within a pore size interval of 3.3–9.4 nm while the bond sizes inferred from the DB curve extend from 3.5 to 6.6 nm. This is a possible indication that the mesoporous glass substrate is compatible with the structure of a type IV or V porous solid [5]. The vapor percolation process observed in these scanning curves is in reality due to the interconnection characteristics of the void network made of sites and bonds. A second important realization is the fact that scanning curves reflect the fact that

Table 3
Pore structure parameters of mesoporous glasses determined from N_2 sorption

Sample	A_{BET} ($m^2\,g^{-1}$)	A_t ($m^2\,g^{-1}$)	V^p ($mm^3\,g^{-1}$)	V^m ($mm^3\,g^{-1}$)	ε	d_m (Å)
SiO_2–Cu	843.6	843.6	958	0	0.68	68
SiO_2–Fe	787.4	787.4	1163	0	0.72	89
SiO_2–diol	413.1	413.1	1382	0	0.75	201

A_{BET} is the BET surface area, A_t the *t*-surface area, V^p the pore volume evaluated at $p/p^0 = 0.99$, V^m the volume of micropores, ε the porosity, and d_m is the mean pore diameter calculated as $d_m = 6V^p/A_{BET}$ (sites assumed as spherical cavities).

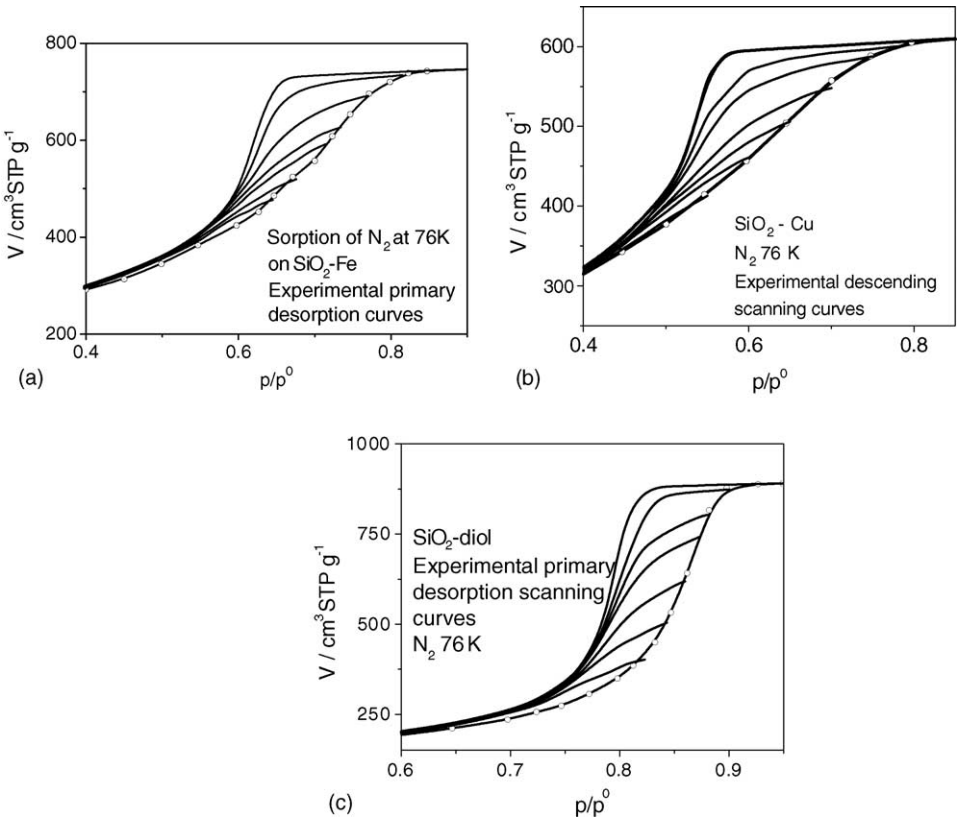

Fig. 13. N_2 primary desorption scanning curves on mesoporous glasses.

pore-blocking effects less affect pores that are being emptied of condensate along a PDS path. Fig. 14b shows the PSDF's calculated from the AB curve and two scanning curves, one having an inversion point at $p/p^0 = 0.70$ and another one at $p/p^0 = 0.75$. The PSD obtained from the PDS with lower reversal point ($p/p^0 = 0.70$) is closer to the PSD obtained from the AB isotherm; on the other hand the curve started at a higher reversal point ($p/p^0 = 0.75$) displays a sharper peak. This means that most pores lodging condensate at $p/p^0 = 0.70$ are still enjoying of a relatively free pathways to the vapor phase when the inversion point is $p/p^0 = 0.70$, however this is not the case for voids holding condensate at $p/p^0 = 0.75$, since these entities will be facing pore-blocking effects during an interval of relative pressures when trying to dislodge their condensate along the descending scanning path.

Fig. 14c illustrates in a PSD diagram several zones of sorption behavior of pores located in sample SiO_2–diol. PSD calculated by the DFT method to AB, DB, and two PDS curves with reversal points at $p/p^0 = 0.87$ and 0.89 render account of several types of behavior. Pore-blocking, vapor percolation, or pores remaining open at the points of reversal of sorption curves are therein illustrated.

3.4. Microporous silica

The whole assortment of N_2 sorption isotherms measured on the series of microporous silica samples synthesized in this work corresponded to type I curves (see Fig. 15). The samples showed practically neither mesopores nor macropores and according to the results of α_S-plots [51] these substrates depicted two micropore classes (see Fig. 16): *ultramicropores* (voids of size smaller than 0.7 nm) and *supermicropores* (voids having sizes between 0.7 and 2 nm) [32]. The isotherm of α-quartz also shown in Fig. 15 is a IUPAC type II curve, since this material was chosen as the reference non-porous adsorbent required to perform the α_S method. Then again due to the microporous essence of the SiO_2 samples, the α_S-plots illustrate two kinds of behavior [51]: a primary filling process occurring at very low pressures and due to the very strong adsorption of molecules in the ultramicropores, and a secondary process in which the supermicropores are being occupied by condensate by reason of the cohesive forces arising between the adsorbed and upcoming molecules. The primary mechanism is linked to the very steep initial aspect of the adsorption curve (i.e. the ultramicropores are being filled when $p/p^0 < 0.01$) while the secondary one reflects a more gradual filling of the pore space (supermicropores) and is responsible of the rounded shape attained by the isotherm knee.

Table 4 shows pore structure parameters corresponding to the microporous SiO_2 samples. There it can be seen that all samples depict a large superficial areas (500–700 $m^2\ g^{-1}$) and significant micropore volumes (300–360 $mm^3\ g^{-1}$). Choosing the density of amorphous silica as 2.2 $g\ cm^{-3}$ the poros-

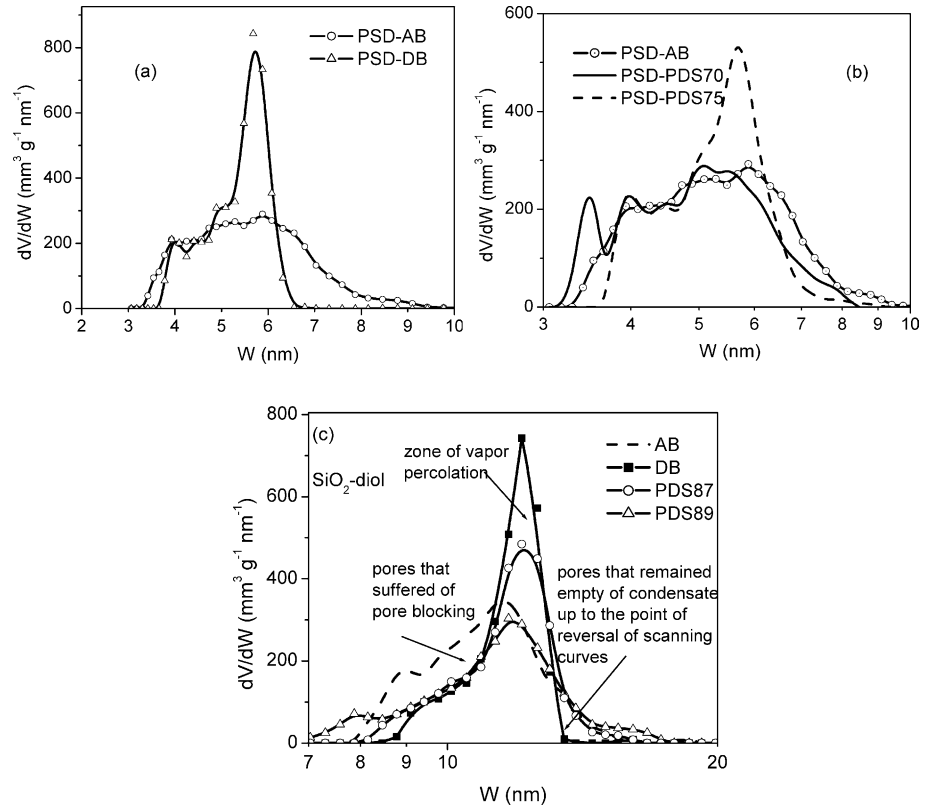

Fig. 14. (a) PSD DFT analysis of AB and DB curves of SiO_2–Cu mesoporous glass calculated from the DFT treatment. (b) DFT analysis of AB, PDS70, and PDS75 paths on sample SiO_2–Cu. (c) PSD for sample SiO_2–diol calculated from AB and DB curves as well as from two desorption scanning curves to illustrate different qualities of pore entities.

ity of these simples oscillates between 0.40 and 0.47; these values are an indication of the fine capacity of these adsorbents to capture molecules of organic or inorganic vapors in their interiors. Furthermore, the volumetric preponderance of supermicropores over ultramicropores would guarantee the eventual release of the trapped substances, since adsorption in ultramicropores is very strong and sometimes the adsorbed molecules are irreversibly retained. Therefore, this kind of microporous substrates would be very adequate for transporting in a safe manner considerable amounts of volatile organic compounds [52] that can be employed after their release from the supermicropores by thermal treatment or some other suitable operation.

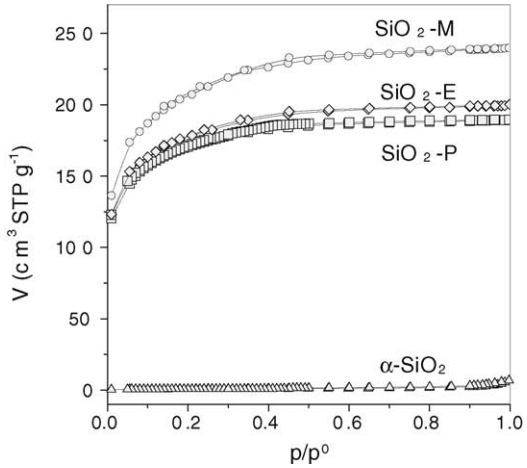

Fig. 15. N_2 sorption isotherms on microporous SiO_2 samples and on a reference, non-porous solid (α-SiO_2).

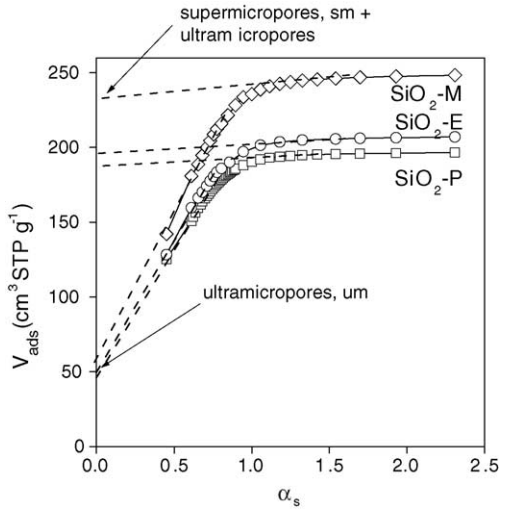

Fig. 16. α_S-Plots obtained from N_2 adsorption on microporous SiO_2 substrates and showing the amounts of supermicropores and ultramicropores.

Table 4
Pore structure parameters of microporous silica samples

Sample	A_{BET} ($m^2\ g^{-1}$)	$W_{0\alpha_S}$ ($mm^3\ g^{-1}$)	W_{um} ($mm^3\ g^{-1}$)	W_{sm} ($mm^3\ g^{-1}$)
α-SiO_2	2.680	0	0	0
SiO_2–P	533.6	297	76	221
SiO_2–E	613.4	310	68	242
SiO_2–M	717.7	358	61	297

α-SiO_2 is the α-quartz reference material, A_{BET} the BET area, $W_{0\alpha_S}$ the total micropore volume, W_{um} the ultramicropore volume, and W_{sm} is the supermicropore volume. All micropore volumes were obtained from α_S-plots.

4. Conclusions

A diversity of mesoporous and microporous materials can be synthesized by the sol–gel and micelle-templating techniques. The SiO_2 solids studied here can be considered as model porous structures due to the following characteristics:

- The SBA-16 substrate is made of interconnected spherical cavities delimited by narrow necks; the sizes of these cavities can be confidently determined from the analysis of the adsorption boundary branch of the hysteresis loop. The adsorption potential plays a significant role during adsorption on these cavities so that DFT or BdB treatments should be employed to perform pore size and pore area analyses. The BdB–BJH pore size corresponds very closely (8.9 nm versus 9 nm) to the micelle hard core of the F127 Pluronic surfactant employed for the synthesis of this substrate. The adsorption potential-corrected Kiselev equation renders a surface area very close to the *t*-plot value. Cavitation arises at some point of the DB curve thus avoiding the possibility of calculating throat sizes from sorption data.
- The SBA-15 porous solid is a sample made by a coacervate of independent cylindrical pores. The pore-size distribution analyses of ascending and descending boundary curves are in satisfactory agreement with each other and with XRD results. The difference between the AB and DB pore size results can be caused by some irregularity of the cross-sectional area of the cylinders as well as by some bending of these pores.
- Mesoporous glasses can provide hysteresis loops of H2 or H1 shapes depending on the addition or not of polyvalent ions (i.e. Cu^{2+} or Fe^{3+}) during the sol–gel synthesis. Pore sizes can be calculated from the AB curve, since the DB curve includes the outcome of vapor percolation. The sites and bonds that compose these glasses seem to be not too different in sizes; this structural property is the main reason by which controlled porous glasses can be synthesized.
- Microporous glasses with predominant supermicropore sizes and negligible mesopore presence are rigid samples suitable for storing and transporting volatile compounds.

Finally, it is pertinent to mention that this work proves that sol–gel preparations can render either microporous or mesoporous substrates depending on the amounts and type of reactants involved in their syntheses and also on the thermal conditions at which the xerogels are obtained.

References

[1] R.K. Iler, The Chemistry of Silica, John Wiley and Sons, New York, 1979.
[2] J.V.L. Beckers, S.W. de Leeuw, Int. J. Inorg. Mater. 3 (2001) 175.
[3] A.V. Neimark, Colloids Surf. A 187/188 (2001) 1.
[4] K.S.W. Sing, D.H. Everett, R.A.W. Haul, L. Moscou, R. Pierotti, J. Rouquerol, T. Siemieniewska, Pure Appl. Chem. 57 (1985) 603.
[5] V. Mayagoitia, F. Rojas, I. Kornhauser, J. Chem. Soc. Faraday Trans. 1 (84) (1988) 785.
[6] V. Mayagoitia, F. Rojas, I. Kornhauser, H. Pérez-Aguilar, Langmuir 13 (1997) 1327.
[7] T. Shimada, K. Aoki, Y. Shinoda, T. Nakamura, N. Tokunaga, S. Inagaki, T. Hayashi, J. Am. Chem. Soc. 125 (2003) 4688.
[8] S. Huh, J.W. Wiench, J.C. Yoo, M. Pruski, V.S.Y. Lin, Chem. Mater. 15 (2003) 4247.
[9] C. Yu, J. Fan, B. Tian, G.D. Stucky, D. Zhao, J. Phys. Chem. B 107 (2003) 13368.
[10] J.M. Kim, Y. Sakamoto, Y.K. Hwang, Y.U. Kwon, O. Terasaki, S.E. Park, G.D. Stucky, J. Phys. Chem. B 106 (2002) 2552.
[11] A. Schreiber, I. Ketelsen, G.H. Findenegg, Phys. Chem. Chem. Phys. 3 (2001) 1185.
[12] M. Imperor-Clerc, P. Davidson, A. Davidson, J. Am. Chem. Soc. 122 (2000) 11925.
[13] J.R. Matos, L.P. Mercuri, M. Kruk, M. Jaroniec, Chem. Mater. 13 (2001) 1726.
[14] A.H. Jansenn, P. Van Der Voort, A.J. Koster, K.P. de Jong, Chem. Commun. (2002) 1632.
[15] Y. Bennadja, P. Beaunier, D. Margolese, A. Davidson, Microporous Mesoporous Mater. 44/45 (2001) 147.
[16] Y. Sakamoto, Y. Kaneda, M. Terasaki, O. Zhao, D. Kim, G.D. Stucky, H.J. Shin, R. Ryoo, Nature 408 (2000) 449.
[17] P. Van Der Voort, M. Benjelloun, E.F. Vansant, J. Phys. Chem. B 106 (2002) 9027.
[18] F. Kleitz, D. Liu, G.M. Anilkumar, I.S. Park, L.A. Solovyov, A.N. Shmakov, R. Ryoo, J. Phys. Chem. B 107 (2003) 14296.
[19] M. Kruk, E.B. Celer, M. Jaroniec, Chem. Mater. 16 (2004) 698.
[20] V. Mayagoitia, F. Rojas, I. Kornhauser, J. Chem. Soc. Faraday Trans. 1 (84) (1988) 785.
[21] V. Mayagoitia, B. Gilot, F. Rojas, I. Kornhauser, J. Chem. Soc. Faraday Trans. 1 (84) (1988) 801.
[22] B.J. Cross, J.M. Haynes, in: S. Modry (Ed.), Pore Structure and Properties of Materials, Akademia, Prague, 1973, p. C61.
[23] S. Okonogi, T. Oguchi, E. Yonemochi, S. Puttipipatkhachorn, K. Yamamoto, J. Colloid Interface Sci. 216 (1999) 276.
[24] W.F. Du, K. Kuraoka, T. Akai, T. Yazawa, J. Phys. Chem. B 105 (2001) 11949.
[25] G. Ge, L. Brus, J. Phys. Chem. B 104 (2000) 9573.
[26] L.D. Gelb, K.E. Gubbins, Langmuir 14 (1998) 2097.
[27] L.D. Gelb, K.E. Gubbins, Langmuir 15 (1999) 305.
[28] L.L. Hench, K.J. West, Chem. Rev. 90 (1990) 33.
[29] D.L. Meixner, A.G. Gilicinski, P.N. Dyer, Langmuir 14 (1998) 3202.
[30] Y. Lu, G. Cao, R.P. Kale, S. Prabakar, G.P. Lopez, C.J. Brinker, Chem. Mater. 11 (1999) 1223.
[31] M. Asomoza, S. Solís, M.A. Hernández, in: B. Haidar (Ed.), Proc. 2nd Int. Conf. Silica Sci. Techn., Inst. Chim. Surf. Interfaces (ICSI-CNRS), Mulhouse, 2001, p. 345.
[32] K. Kaneko, in: W. Rudzinski, W. Steele, G. Zgrablich (Eds.), Equilibria and Dynamics of Gas Adsorption on Heterogeneous Solid Surfaces, Elsevier, Amsterdam, 1994, p. 679.

[33] N.K. Raman, M.T. Anderson, C.J. Brinker, Chem. Mater. 8 (1998) 1682.
[34] R. Vacassy, R.J. Flatt, H. Hofmann, K.S. Choi, R.K. Singh, J. Colloid Interface Sci. 227 (2000) 302.
[35] R.L. Rill, B.R. Locke, Y. Liu, D.H. Van Wink, Proc. Natl. Acad. Sci. U.S.A. 95 (1998) 1534.
[36] J.M. Haynes, in: D.H. Everett, R.H. Ottewill (Eds.), Surface Area Determination, Butterworths, London, 1970, p. 97.
[37] L.D. Sarkisov, P.A. Monson, Langmuir 17 (2001) 7600.
[38] P.I. Ravikovitch, A.V. Neimark, Langmuir 18 (2002) 9830.
[39] E.P. Barrett, L.G. Joyner, P.H. Halenda, J. Am. Chem. Soc. 73 (1951) 373.
[40] J.C.P. Broekhoff, J.H. de Boer, J. Catal. 9 (1967) 8.
[41] A. Domínguez, S. Bories, M. Prat, Int. J. Multiphase Flow 26 (2000) 1951.
[42] S.J. Gregg, K.S.W. Sing, Adsorption, Surface Area and Porosity, Academic Press, London, 1982.
[43] J. Fan, C. Yu, L. Wang, B. Tu, D. Zhao, Y. Sakamoto, O. Terasaki, J. Am. Chem. Soc. 123 (2001) 12113.
[44] J.C.P. Broekhoff, J.H. de Boer, J. Catal. 10 (1968) 368.
[45] P.I. Ravikovitch, G.L. Haller, A.V. Neimark, Adv. Colloid Interface Sci. 76/77 (1998) 203.
[46] P.I. Ravikovitch, A.V. Neimark, J. Phys. Chem. B 105 (2001) 6817.
[47] M. Kruk, M. Jaroniec, Langmuir 15 (1999) 5279.
[48] D.H. Everett, J. Colloid Interface Sci. 52 (1975) 189.
[49] J.M. Esparza, M.L. Ojeda, A. Campero, A. Domínguez, I. Kornhauser, F. Rojas, Colloids Surf. A 241 (2004) 35.
[50] F. Rojas, I. Kornhauser, J. Salmones, S. Cordero, J.M. Esparza, C. Felipe, in: F. Meunier (Ed.), Fundamentals of Adsorption, vol. 6, Elsevier, Paris, 1998, p. 327.
[51] R.A. Roberts, K.S.W. Sing, V. Tripathi, Langmuir 3 (1987) 331.
[52] J. Sun, T.D. Jarvi, L.F. Conopask, S. Satyapal, Energy Fuels 15 (2001) 1241.